

Disentangling degenerate solutions from primary transit and secondary eclipse spectroscopy of exoplanets

Caitlin A. Griffith¹

ABSTRACT

Infrared transmission and emission spectroscopy of exoplanets, recorded from primary transit and secondary eclipse measurements, indicate the presence of the most abundant carbon and oxygen molecular species (H_2O , CH_4 , CO , and CO_2) in a few exoplanets. However, efforts to constrain the molecular abundances to within several orders of magnitude are thwarted by the broad range of degenerate solutions that fit the data. Here we explore, with radiative transfer models and analytical approximations, the nature of the degenerate solution sets resulting from the sparse measurements of “hot Jupiter” exoplanets. As demonstrated with simple analytical expressions, primary transit measurements probe roughly 4 atmospheric scale heights at each wavelength band. Derived mixing ratios from these data are highly sensitive to errors in the radius in planet (at a reference pressure), which are approximately a few percent. For example, an uncertainty of 1% in the radius of a 1000 K and H_2 -based exoplanet with Jupiter’s radius and mass, causes an uncertainty of a factor of ~ 100 -10000 in the derived gas mixing ratios. The degree of sensitivity depends on how the line strength increases with the optical depth (i.e. the curve of growth) and the atmospheric scale height. Temperature degeneracies in the solutions of the primary transit data, which manifest their effects through scale height and absorption coefficients, are smaller. We argue that these challenges can be partially surmounted by a combination of selected wavelength sampling of optical and IR measurements and, when possible, the joint analysis of transit and secondary eclipse data of exoplanets. However, additional work is needed to constrain other effects, such as those due to planetary clouds and star spots. Given the current range of open questions in the field, both observations and theory, there is a need for detailed measurements with space-based large mirror platforms (e.g. JWST) and smaller broad survey telescopes, as well as ground-based efforts.

Subject headings: extrasolar planets; exoplanets; planetary atmospheres; radiative transfer; atmospheric structure

¹Univ. of Arizona, Dept. of Planetary Sciences, LPL, 1629 E. Univ. Blvd, Tucson, AZ 85721-0092; griffith@lpl.arizona.edu

1. Introduction

Over 800 planets have been detected outside the Solar System. Current statistics show that planets are common; data from the Kepler Mission indicate that more than half of all stars have planets (Fressin et al. 2013). Planets range in size, encompassing Earth to Jupiter diameters. Most of these planets are smaller than Uranus; and terrestrial-sized planets are predicted to orbit one sixth of all stars (Fressin et al. 2013). However the majority of spectroscopically measured planets are predominantly Jovian-sized and hot ($T_{eff} \sim 700\text{-}3000$ K). It is largely, although not exclusively, through studies of these “hot Jupiters and Neptunes” as well as hot ($T_{eff} \sim 500$ K) “super-Earths” that techniques for measuring and retrieving compositional and structural information are currently tested. These techniques open the field of planetary sciences to the larger questions about planets related to their diversity, the physical processes that control their characteristics in different stellar environments, and the uniqueness of the Solar System and life.

Studies of exoplanetary atmospheres began with observations of transiting planets (now over 230 of them), particularly the two bright exoplanet systems HD 209458b and HD 189733b. The first detection of a planetary atmosphere came from the analysis of optical spectra of HD 209458b as it passed in front of its host star (Charbonneau et al. 2000). The planet’s sodium resonance doublet at 589.3 nm was revealed from the attenuation of the star’s light through the planet’s atmosphere at the limb. Primary transit measurements of HD 189733b at near-IR wavelengths displayed features indicative of the presence of water, consistent with its expected large abundance and dominant role in the spectra of hot Jupiter exoplanets (Tinetti et al. 2007; Grillmair et al. 2008). Thermal emission was first detected from measurements of HD 209458b’s passage behind its star during secondary eclipse. The planet plus star’s 4.5 μm (Charbonneau et al. 2005) and 8 μm (Deming et al. 2005) emissions were compared to those of the star alone, yielding a brightness temperature close to the current expected value of 1130 K (Fortney et al. 2005). Observations of exoplanetary transmission and emission spectra recorded during the primary transit and secondary eclipse, complement each other, as the former is sensitive to the planet’s composition and not so much to the thermal profile, and the latter is sensitive to both of these planetary characteristics.

Currently, photometry and spectroscopy of transiting exoplanets indicates the presence of water, methane, carbon monoxide and carbon dioxide in a number of extrasolar planets, (e.g. Tinetti et al. 2007, Grillmair et al. 2008, Madhusudhan & Seager 2009, Swain et al. 2008, Swain et al. 2009b, Snellen et al. 2010). Observations at different points in an exoplanet’s orbit also reveal variations in the planet’s the temperature field with longitude, which indicate the planet’s dynamical redistribution of heat, (e.g. Harrington et al. 2006, Knutson et al. 2007, Crossfield et al. 2010, Knutson et al. 2012). Yet even for the brightest systems, molecular abundances are constrained only to within 3-5 orders of magnitude and temperatures as a function of pressure constrained to roughly 300 K, (e.g. Madhusudhan & Seager 2009, Lee et al. 2012, Line et al.

2012). The lack of precision in the derived characteristics results in part from systematic errors and noise commensurate with the small signal of the planet, and for certain systems from the host star’s variability. Yet many of the uncertainties in the derived composition and thermal structure of exoplanets, at present, stem from the range of models that fit the data, (e.g. Swain *et al.* 2009a, Madhusudhan & Seager 2009, Madhusudhan *et al.* 2011, Benneke & Seager 2012, Lee *et al.* 2012, Line *et al.* 2012, Griffith *et al.* 2013).

Emission spectra, recorded during the secondary eclipse, can be interpreted with a range of temperature and composition profiles. Ultimately, if in local thermodynamic equilibrium (LTE), the absorbing gases must have abundances that cause emission from pressure levels where the temperature approximates the observed brightness temperature. This dependency leads to a number of degenerate solutions where the derived gas abundances correlate with the derived temperature profiles (Swain *et al.* 2009; Madhusudhan & Seager 2009; Lee *et al.* 2012; Line *et al.* 2012).

Light curves recorded during the primary transit measure the ratio of the planet to star areas, revealing the transmission of the light through the limb of the planet’s atmosphere. These measurements probe the planet’s composition, clouds, and the surface pressure (Seager & Sasselov 2000; Brown 2001; Benneke & Seager 2012). The retrieved gas abundances depend on the atmospheric temperature through the occupation of states, doppler line broadening, and the atmospheric scale height $H = R_g T / \mu g$.¹ The derived abundances are thus affected by the mean molecular weight of the atmosphere (Miller-Ricci *et al.* 2009), as well as the surface pressure and radius as a function of pressure (Tinetti *et al.* 2010; Benneke & Seager 2012). Particularly for the low spectral resolution observations currently possible, these dependences lead to the derivation of a range of temperature and composition profiles.

Here we explore the degenerate solutions of hot Jovian exoplanets, where the mean molecular weight is assumed to be dominated by hydrogen and helium, and any surface lies too deep to be detected. These assumptions pertain to all of the exoplanets extensively measured to date, with the possible exception of the “super-Earth” exoplanet GJ1214b (Miller-Ricci *et al.* 2009). With this simplification, mainly the thermal profile, the abundances of the major carbon and oxygen molecules, and the planetary radius affect the analysis of infrared measurements of the primary transit and secondary eclipse. These characteristics are therefore the main observables. Other characteristics of the planet, (e.g. clouds, minor species, and non-LTE emission), and the host star (e.g. star spots) can also play a significant role in the interpretation of exoplanetary data, and will be discussed briefly at the end of the paper. Yet currently, even ignoring these other characteristics,

¹Here R_g is the gas constant, T the temperature, μ the mean molecular weight and g the gravity. The scale height is a measure of the e-folding height of the atmospheric pressure at constant temperature, i.e. the puffiness of the atmosphere.

there is too little data of high enough caliber, wavelength coverage and reproducibility to strongly constrain the characteristics of exoplanetary atmospheres, largely because of the degeneracies in the solution set.

In order to investigate the solution sets and information content of low resolution optical and near-IR measurements of exoplanetary atmospheres, we discuss the analysis of data of XO-2b, which has not been extensively measured. Thus the sources of the degeneracies are more obvious. The effects of the temperature and radius on the derived composition are found to depend on the planet’s atmospheric scale height and can therefore be estimated analytically for any extrasolar planet. Analytical approximations, tested against a full set of radiative transfer models of data from the exoplanet XO-2b, indicate that an uncertainty in the planet’s radius of 1% causes the gas mixing ratios derived from primary transit data to be uncertain by several orders of magnitude, depending on the atmospheric scale height and the line regime. The analysis is not sensitive, separately, to uncertainties in the host star’s radius, because primary eclipses measure the ratio of the planet to star radii. Thus the derived planet’s radius scales to the assumed stellar radius, which must be indicated. In this study XO-2b’s host star radius is assumed to be $0.964 R_{Sun}$, (Burke et al. 2007), where $R_{Sun} = 695500$ km. This degeneracy and less so that introduced by uncertainties in the temperature, hamper the derivation of compositional information from primary transit data. In contrast, the largest correlations in the solution set of secondary transit data concern the thermal profile and composition; these degeneracies also yield abundances that range several orders of magnitude.

However for planets in which both primary and secondary eclipse data are possible, the joint analysis of both measurements decorrelates the radius and temperature and composition structures. Here we assume that the compositional and thermal differences between the sampled dayside and terminator atmospheres can be constrained, as discussed further below. The analysis of XO-2b’s sparse data indicates that the composition and thermal profile solution sets from primary and secondary eclipse data are significantly distinct that the combined analyses of these data yield stronger constraints on a planetary structure (Griffith et al. 2013). Degenerate solution sets of primary and secondary eclipse are considered in detail to explore the correlation between the parameters that lead to viable interpretations of current transit data.

2. LTE models of exoplanetary atmospheres

A number of different techniques are used to extract composition and temperature information from secondary eclipse data. All models start with basic assumptions regarding the number and identity of gases that affect the spectrum, and the temperature parameters that characterize the thermal profile. The most basic extraction technique selects a phase space of all the potential mix-

ing ratios and temperature profiles sampled at a fine enough grid to characterize the data within the errors (Madhusudhan & Seager 2009; Griffith et al. 2013). Another technique, the Markov chain Monte Carlo (MCMC) method, similarly explores a phase space of potential solutions, calculates the spectrum, and compares this to the data. However, this method does not directly calculate all of phase space. Instead it randomly jumps through while mostly accepting the jumps that improve the fit to the data, thereby converging to the solution sets more quickly (Madhusudhan et al. 2011; Benneke & Seager 2012). Another approach, Optimal Maximization, inverts the data using an iterative scheme to maximize the probability of attaining the best solutions to the data (Rodgers 2000; Lee et al. 2012; Line et al. 2012). These models converge to a best solution. Here we adopt the first technique described above – the brute force exploration of all of the defined phase space with millions of models. The advantage of this approach is that the analysis of both primary transit and secondary eclipse can be explored with the same parameter space or one altered to account for the differences in temperature and composition between the dayside and terminator atmospheres. After the spectrum of each model is computed, a principal components analysis (PCA) determines the strongest correlations between the parameters in the solution set and thereby the linear combination of the parameters that drive it.

In this paper we consider, as an example, an analysis of the exoplanet XO-2b, which is among the more extensively observed “hot Jupiters” in the sense that XO-2b is one of the few planets with a Hubble Space Telescope (HST) primary transit spectrum from 1.2-1.8 μm (Crouzet et al. 2013) and secondary eclipse photometry from the space-based Spitzer telescope (Machalek et al. 2009). XO-2b orbits a K0V star 0.0369 ± 0.002 AU away, which forms a binary system with a companion K0V star roughly 4600 AU from the host star (Burke et al. 2007). The metallicity of this system is well established, with measurements of both stars indicating the same composition within errors; the abundances of iron, nickel, carbon and oxygen are enhanced above solar (Teske et al. 2013a). With a 2.6 day period, XO-2b is a Jupiter-sized ($0.996 R_J$) planet, although slightly less massive ($0.5 M_J$) (Burke et al. 2007; Fernandez et al. 2009).

2.1. Secondary Eclipse Measurements

Emission spectra of planetary atmospheres in LTE are controlled by the atmospheric temperature and opacity profiles. Likewise the thermal profile manifests the heating and cooling processes in the atmosphere. Hot Jupiter exoplanets, similar to the atmospheres of the giant planets, are expected to have a convective region heated by the interior. However unlike the giant planets in the Solar System, for which the radiative-convective boundary lies at ~ 1 bar, the highly irradiated hot Jupiters have boundaries at ~ 100 bars. The high optical depths in the region above this level in a hot Jupiter give rise to an isothermal region where radiative transfer proceeds by diffusion.

Consistent with model predictions (Fortney et al. 2005), this stable region exists up to the pressure level (~ 1 -10 bars) where the atmosphere starts to become optically thin. Above this level, the atmosphere cools radiatively, which causes the temperature to decrease with height, like the terrestrial troposphere. If higher up in the atmosphere there is a decrease in radiative cooling and/or an increase in heating, then the atmosphere’s temperature increases, thereby creating a temperature inversion, similar to the stratosphere on Earth. For example, stratospheres form from the decrease in the pressure induced absorption with height, and through the presence of high altitude photochemical haze and other optical absorbers. These pressure-temperature regimes can be identified in theoretical models of the thermal profiles of the most extensively observed exoplanets HD 209458b and HD 189458b (Fig. 2).

The presence of spectral features and their nature, i.e. whether they appear as an emission or absorption feature, depend on the slope of the section of the thermal profile being sampled. If the temperature decreases with height, an absorption feature causes a decrease in emission; conversely if the temperature increases with height; an absorption feature causes an increase in emission. No features are formed in a vertically isothermal region. Measurements that sample both the stratosphere and troposphere of an atmosphere are difficult to interpret because an absorption feature can increase, decrease, or not affect the planet’s outgoing intensity, depending on where it forms. Most notably, interpretations of measurements of emission data of HD 209458b indicate either water features from the stratosphere (Burrows et al. 2007) or mainly methane absorption coupled with water from the troposphere (Swain et al. 2009). The former interpretation (Burrows et al. 2007) however can not explain the Spitzer 24 μm measurement, and has most of the exoplanet’s radiation emitted from the stratosphere. It turns out that an inverted water spectrum can (with sparse data) resemble a methane spectrum over certain wavelength regions and at low spectral resolution. However, in general most of the radiation from an exoplanet in the wavelength region of highest emission (i.e. near 3 μm for a $T_{\text{eff}}=1000$ K planet) comes from the region where the temperature decreases with height due to radiative cooling.

With the cautionary note that constraints on the composition and structure of an exoplanet depend on the spectral modulation of its features, the signal-to-noise, and the spectral resolution and coverage, here we examine, for the purpose of providing a simple example, an analysis of Hubble Space Telescope (HST) photometric measurements of XO-2b at 3.6, 4.5, 5.8 and 8.0 μm (Machalek et al. 2009). With such little data, only a simple atmospheric profile with no stratospheric inversion is considered here, which is consistent with theoretical calculations of the close analog system, HD 189458b (Grillmair et al. 2008; Madhusudhan & Seager 2009; Lee et al. 2012). Models with temperature inversions are discussed in (Griffith et al. 2013). The emission points are interpreted with a radiative transfer model that assumes LTE, and includes the opacity of H_2O , CO, CH_4 , CO_2 and pressure-induced H_2 . As discussed in more detail in Griffith *et al.* 2013, line-by-line calculations of the HITEMP line parameters (Rothman et al. 2009) are used to calculate

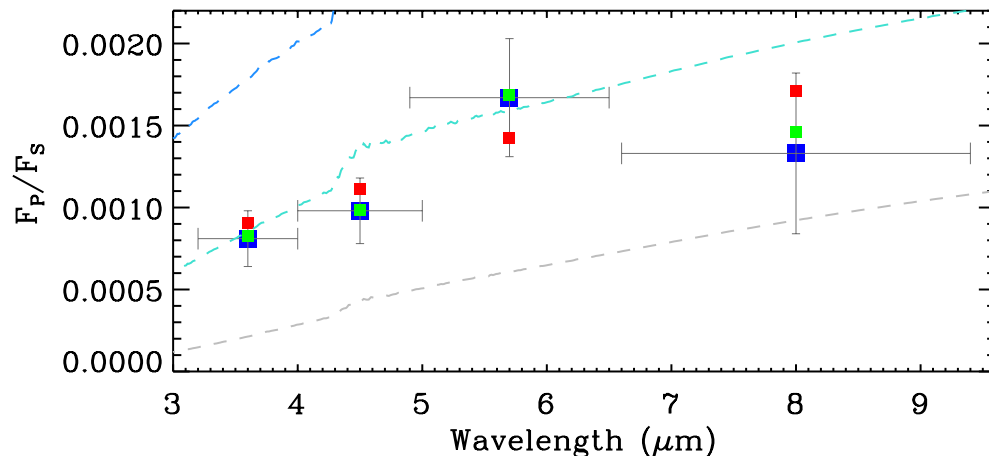


Fig. 1.— SPITZER photometry measurements (Machalek et al. 2009) of the ratio of XO-2b’s flux to that of its host star (blue squares), compared to a couple of models (red and green). Blackbody fluxes at 1000, 1500 K are shown in gray and cyan. Adopted from (Griffith et al. 2013).

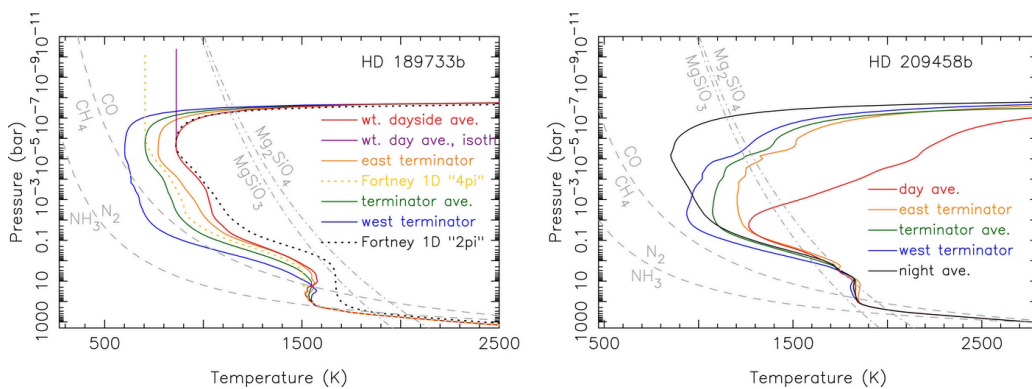


Fig. 2.— Temperature-pressure profiles of exoplanets HD 189733b and HD 209458b for the model atmospheres of Moses *et al.* 2011, based on the radiative transfer models of Fortney *et al.* 2006 and Fortney *et al.* 2010, and the GCM models of Showman *et al.* 2009. Figure taken from Moses *et al.* 2011.

k-coefficients of CO. For CH₄ and H₂O, k-coefficients were calculated from the absorption coefficients derived by Freedman *et al.* (2008); absorption by CO₂ lines derive from line-by-line calculations of the CDSO data base (Tashkun *et al.* 2003). However, for CH₄, at wavelengths below 3 μm, we increase the methane absorption by a factor of 10 to fit the laboratory data at 2.2 and 1.7 μm (Nassar & Bernath 2003; Thiévin *et al.* 2008).

The temperature profile was parametrized with 4 variables in order to explore a range of profiles.² The mixing ratios are assumed constant, which is the expected profile for H₂O and CO, and a reasonable one for CH₄ and CO₂ (Moses *et al.* 2011), since the data sample only a small pressure region (Fig. 3). Mixing ratios ranging from 10⁻³–10⁻⁸ were considered for each molecule, except for CO₂ which ranges 10⁻⁴–10⁻⁸, because it is expected to be significantly less abundant (Moses *et al.* 2011). Based on the planet’s density, the atmosphere is taken to be mainly hydrogen and helium with Jovian mixing ratios. Radiative transfer calculations derive the flux at the 4 measured photometry points, integrated over each Spitzer filter bandpass for each model atmosphere. Given the range and sampling of gas mixing ratios and the thermal profile parameters a total of almost 82 million non-inversion models were calculated and compared to the data. (The original study also includes temperature inversions (Griffith *et al.* 2013).) The goodness of fit is evaluated with a weighted mean square error, ϵ , such that:

$$\epsilon = \frac{1}{N} \sum_{i=1}^N \left(\frac{F_i^{model} - F_i^{obs}}{\sigma_i} \right)^2$$

where F_i^{obs} is the observed planet flux to star flux ratio at i^{th} wavelength in the spectrum, F_i^{model} is the calculated value, and σ_i is the 1 sigma error in the measured value (Madhusudhan & Seager 2009). However, since the errors do not necessarily follow a gaussian distribution, we keep all models that fit the data within the errors.

While none of the parameters are constrained, only 3% of the explored phase space yielded models that fit all 4 emission points within the errors. In addition, the parameters of the successful models are highly correlated. As shown in figures 3–4, the abundance of water, which controls most of the opacity, tracks with the pressure level of the 1500 K atmospheric level. The abundance of methane also plays a large role in the models that fit the data, while CO and CO₂ similarly influence only the interpretation of the 4.5 μm measurement (Fig. 3). These correlations in fact drive the population of the solution, as can be seen from the principal component and secondary component of the Principal Component Analysis (PCA) of solution set, which line up with the

²The thermal profile parameters are the temperatures of the troposphere, T_T , and deep isothermal atmosphere, T_I , and the pressures of the tropopause, P_T , and the top of the lower isothermal region, P_I , following (Madhusudhan & Seager 2009). The range of values considered are, respectively, 600-1300 K, 1300-3100 K, 0.1–10⁻⁵ bar and 1–10 bar. In total 2880 profiles were calculated.

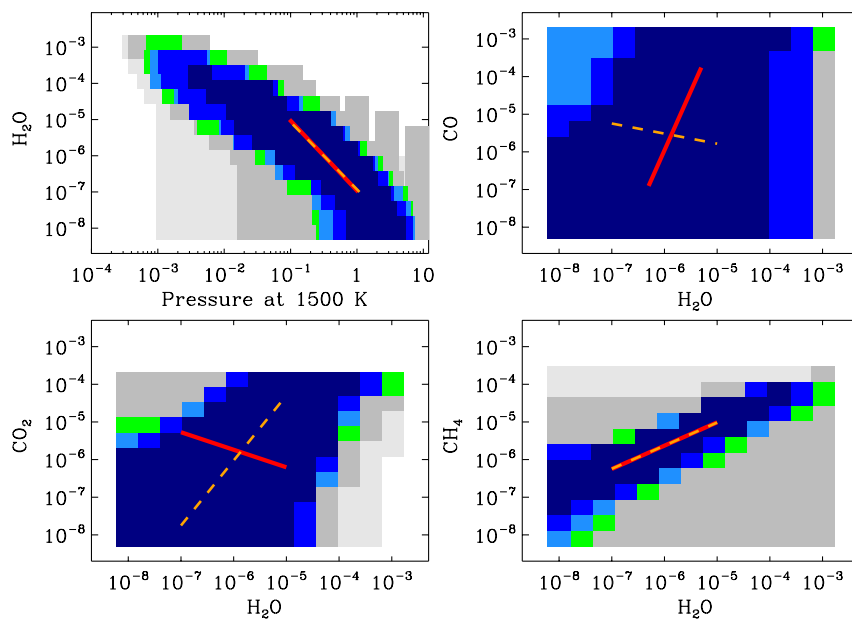


Fig. 3.— Models that match XO-2b’s secondary eclipse data within the errors are shown for two model parameters in each panel. Colors represent the degree to which the models match the data; navy blue, blue, light blue, green, and grey correspond to weighted arithmetical mean square errors increasing respectively from 0.2 to 0.5; light grey indicates values above 0.5. Navy blue models most closely match the data. Red and orange lines mark the projection of the principal and secondary axes of the principal component analysis of the solution set as described in Griffith *et al.* 2013. Credit: Griffith *et al.* 2013.

apparent correlations in the gas abundances (Fig. 3). Note that abundances of CO and CO₂ compete in establishing the 4.5 μm measurement, and establish the secondary component correlation. The PCA analysis is discussed in more detail by Griffith *et al.* (2013).

This solution is not surprising; essentially, the mixing ratios fit the data as long as the temperature profile is adjusted so that the outgoing intensity is equivalent to the measured brightness temperature of 1000–1600 K (Fig 1). The other gases track loosely with water, with the exception of CO₂ and CO, which has little effect on the spectrum. Similar trends are detected in the analyses of the HD 209458b (Swain *et al.* 2009). However with such sparse data, no constraints could be derived for individual parameters, i.e. those that define the thermal profile and the composition. For example, atmospheres with and without thermal inversions fit the data (Griffith *et al.* 2013). The addition of a temperature inversion of, for example, 800 K leads to additional peaks in the contribution functions and therefore separate sets of correlated solutions associated with each stratospheric profile (Griffith *et al.* 2013).

2.2. Primary Transit Data

During primary transit the star’s light drops by a factor equal to the ratio of the planet to star’s effective areas. The depth of the resulting light curve at each wavelength, often termed “absorption”, can be written (Brown 2001) as:

$$A = \frac{\pi R_p^2}{\pi R_s^2} + \int_{R_p}^{\infty} 2\pi R(1 - Tr(R))dR / \pi R_s^2. \quad (1)$$

Here R_p is the radius of the planet at a specified pressure P_0 (e.g. 10 bars) where the planet is opaque; R_s is the primary star’s radius; and $Tr(R)$ is the atmospheric transmission at the particular wavelength of light through a chord that is a distance R from the planet’s center, referred to here as the impact radius (Fig. 5). The first term represents the occultation of the opaque part of the planet at pressures greater than P_0 . For a Jupiter-sized body orbiting a solar-sized star, this term causes a ~1% drop in the light of the star. The second term represents the occultation of the planet’s atmosphere, which causes a drop of ~0.2% or less, depending on the atmospheric scale height. Note that Equation 1 assumes that all the chords at an impact radius R intersect the same atmosphere, although there are likely latitudinal and longitudinal variations in composition, temperature and cloud cover (Cho *et al.* 2003; Showman *et al.* 2009; Fortney *et al.* 2010).

The atmospheric transmission for a specified wavelength, $Tr(R)$, of light through a chord, s , that is a distance R from the planet’s center can be expressed as:

$$Tr(R) = \exp \left(- \int_s N(r(s)) \kappa_e(r(s)) ds \right) \quad (2)$$

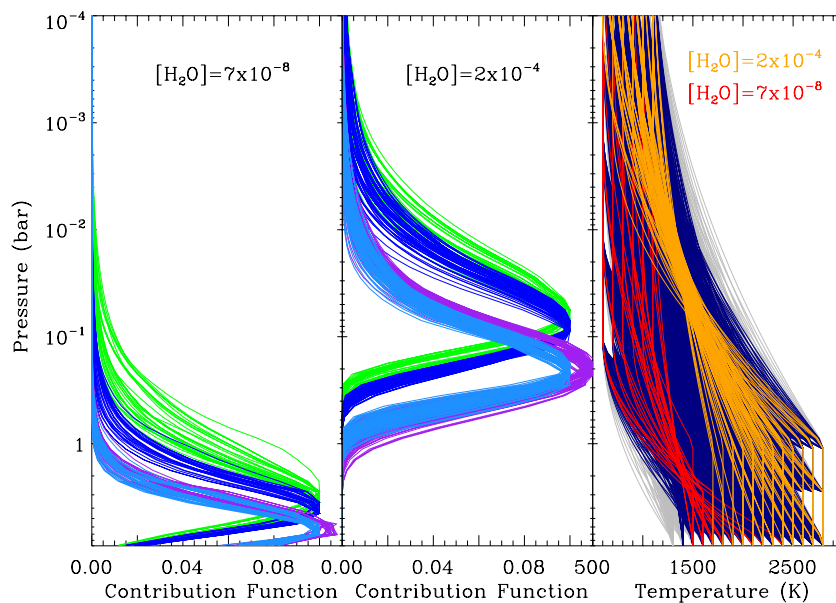


Fig. 4.— Right Panel: Most temperature profiles (blue) of the non-inversion models (grey) fit the data. The profiles separate into different subsets that depend on the model’s water abundance, which dominates the opacity. This effect is shown for models with $[\text{H}_2\text{O}] = 7 \times 10^{-8}$ and $[\text{H}_2\text{O}] = 2 \times 10^{-4}$. In each case, the contribution functions peak at the pressure level where the temperature is ~ 1500 K. The water abundance establishes the pressure level where most of the emission derives, as indicated by the contribution models for the two water abundances. Contribution functions are shown for all the temperature profiles that fit the data at the Spitzer wavelengths of 3.6, 4.5, 5.8, and 8.0 μm , in light blue, purple, blue and green, respectively. Credit: Griffith *et al.* 2013.

where $r(s)$ is the distance to the center of the planet at a point along the tangent, $N(r(s))$ is the atmospheric density at s , and κ_e is the extinction of all sources of opacities at the specified wavelength (Fig. 5). All scattered radiation is assumed to leave the beam; thus κ_e includes extinction due to both gas absorption and particle scattering. The optical depth is derived to the needed precision by dividing the tangential path into infinitesimal lengths, ds , and calculating the column abundance, $N(s)ds$, of the discrete bits of atmosphere, which when summed provide the total tangential column density, $N_t(R)$ at the impact radius R .

As shown in past studies (Tinetti et al. 2010; Benneke & Seager 2012), the analysis of primary transit data requires constraints on the temperature and radius at a specified pressure level. Before discussing the joint analysis of the primary transit and secondary eclipse data, we calculate the sensitivity of the derived mixing ratios on the planet’s temperature and radius.

3. Primary Transit Measurements

3.1. Approximate Eclipse Depth

To develop an intuition of the nature of exoplanet transmission spectra, we work with an analytical approximation of the transmission of light through the planet’s limb (Chamberlain & Hunten 1988). The extinction coefficient, κ_e , is assumed to equal that at the impact radius, i.e. $\kappa_e(s(r)) = \kappa_e(R) \forall s(r)$. The integral of the density along tangent line, s , an infinite distance in either direction,

$$N_t(R) = \int_{-\infty}^{\infty} N(r(s)) ds,$$

is approximated by assuming that the temperature along the chord is constant (Fig. 5). The value of $N(r)$ can then be expressed in terms of that at the impact radius, R :

$$N(r) = N(R) e^{-(r-R)/H}, \quad (3)$$

where H is the atmospheric scale height. The resulting integral is a modified Bessel function of the third kind, K_1 , which has a series solution³. Keeping only the first term:

$$N_t(R) \approx N(R) (2\pi RH)^{1/2}. \quad (4)$$

This approximation is reasonably reliable because most of the contribution to the optical depth derives from the closest point of the tangent line from the center of the planet, i.e. the impact

³ Change the dependent variable to β , the angle between R and r (Fig. 5). Then: $r = R \sec\beta$, and $s = R \tan\beta$, and $ds = R \sec^2\beta d\beta$. We find then that : $N_t(R) = \int_{-\pi/2}^{\pi/2} N(R) e^{-R(\sec\beta-1)/H} R \sec^2\beta d\beta$, the solution of which is a modified Bessel function of the third kind, K_1 : $N_t(R) = 2N(R) R e^{R/H} K_1(R/H)$

radius R . Correspondingly, the transmission of the atmosphere through a chord a distance R away from the planet’s center is:

$$Tr(R) = \exp(-N(R) (2\pi RH)^{1/2} \kappa_e). \quad (5)$$

The transmission of the host star’s light through the exoplanet’s limb, i.e. the right-hand integral term in equation 1, is generally approximated as a sum over the impact radius. This sum consists mainly of terms that are either approximately zero or one, corresponding to regions where the chord traverses optically thin ($Tr(R)=1$) and thick ($Tr(R)=0$) slices of the limb, respectively. Basically as the impact radius increases, moving outwards radially, the column density of the cord rapidly transitions from being opaque to optically thin, such that the region where $\delta Tr(R)/\delta P(R)$ peaks is where one is maximally sensitive. Information regarding the exoplanet’s atmosphere can be derived only from the region in the atmosphere where the the transmission through the limb’s chord most dramatically drops in value, e.g. from 5% to 95%.

3.2. Pressure region probed

The pressure range probed by the transmission of light through the limb of an atmosphere is ~ 4 atmospheric scale heights. This is a general result, which we derive by designating R_1 as the impact radius where the transmission through the chord is near one (e.g. $Tr_1 = Tr(R_1)=0.95$) and R_2 the distance where the transmission is near zero (e.g. $Tr_2 = Tr(R_2)=0.05$). The atmospheric region probed is then roughly $\Delta R = R_1 - R_2$. Assume that the atmosphere is isothermal and homogenous within this pressure region; then, since

$$N(R_1) = N(R_2)e^{-(\Delta R)/H}, \quad (6)$$

ΔR can be estimated by dividing $\ln(Tr_1)$ by $\ln(Tr_2)$ using Eq. 5:

$$\Delta R \approx H \ln[\ln(Tr_2)/\ln(Tr_1)].$$

Adopting values of $Tr_1=0.95$ and $Tr_2=0.05$, we find that primary transit observations sample a region of roughly 4 scale heights ($4H$), i.e. a factor of ~ 55 drop in pressure at each wavelength. Of course the atmosphere is not isothermal and homogeneous; this value is more indicative than exact. Therefore it is useful to compare this approximation to the results of a full model of XO-2b’s atmosphere, where the chord’s column abundances, the temperature and pressure values, and their effects on the extinction coefficients are calculated precisely. The full calculation (Fig. 6) indicates that, at a wavelength of $1.56 \mu\text{m}$, the primary transit of XO-2b probes a pressure region corresponding to a factor of 75 change in pressure, equivalent to $4.3H$, i.e. close the the

approximated value above. Given the small extent of the limb that is sampled, the opacity of the atmosphere acts primarily to determine the cutoff radius, R_0 , where the atmosphere becomes optically thick.

3.3. Retrieval dependence on Radius

As shown in Eq. 1, at a given wavelength the contribution of the atmosphere (right hand term) is established by the depth of the lightcurve, $A(\lambda)$, (left hand term) and the assumed radius at a specified pressure, R_p (middle term). The question then arises: how sensitive is the derivation of an exoplanet's composition to the assumed radius, R_p ? Knowledge of the detailed structure of the atmosphere is not needed to approximate this value. Consider the possibility that a given planet has a radius, R_p , at specified pressure (e.g. 10 bars) for which the uncertainty ranges from a large value, R_L , to a smaller value, R_S . One can imagine two model atmospheres where for the R_L model pressures are shifted upward by $\Delta R = R_L - R_S$ in comparison to the R_S model. The ratio of the limb optical depths of the larger to smaller models at an impact radius R is:

$$\frac{\tau(R)_L}{\tau(R)_S} = \frac{N(R)_L (2\pi R H_L)^{1/2} \kappa_L}{N(R)_S (2\pi R H_S)^{1/2} \kappa_S}. \quad (7)$$

At a specific impact radius, R , the integrated traverse column density of the larger radius planet is higher because the pressure is higher. If the extinction coefficients are kept the same, the increased column abundance of the higher radius planet will cause the optical depth of that model to be higher than that of the smaller model at R . To achieve the same light curve, the extinction coefficient of the large radius model must decrease. Assume an isothermal atmosphere such that $H_L = H_S$ and assume a small difference between R_L and R_S . Approximate the density $N(R)_L$ in terms of $N(R)_S$ with Eq. 6; then the ratio of optical depths becomes:

$$\frac{\tau(R)_L}{\tau(R)_S} = e^{(\Delta R/H)} \frac{\kappa_L}{\kappa_S}.$$

To match the observed light curve depth, the traverse optical depth at each impact radius must be equal for both the high and low radius models. Thus $\tau_L(R) = \tau_S(R)$, and

$$\frac{\kappa_L}{\kappa_S} = e^{(-\Delta R/H)} \quad (8)$$

This expression indicates the sensitivity of the derived opacity to an uncertainty of ΔR in the assumed radius. For example, consider an uncertainty of 1% in the planet's radius. This distance corresponds to roughly 4.6 atmospheric scale heights ($H=146$ km), assuming a jovian mass and radius, and a temperature (1000 K) typical of hot exoplanets. In this case, a 1% uncertainty in radius of the planet indicates an optical depth uncertainty of a factor of 100 (Eq. 8).

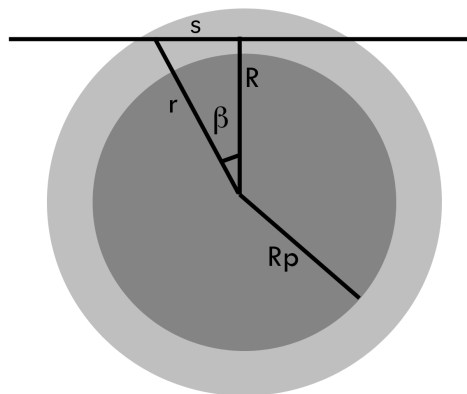


Fig. 5.— During primary transit, the star’s light passes through the limb of the exoplanet. Shown is the path of one ray at an impact radius R . The ray traverses a total column density $N_T(R)$ of atmosphere, given by the density at each point along the chord integrated by ds , the infinitesimal distance. A reference radius, R_p , at a specific pressure is specified where the planet’s atmosphere is opaque.

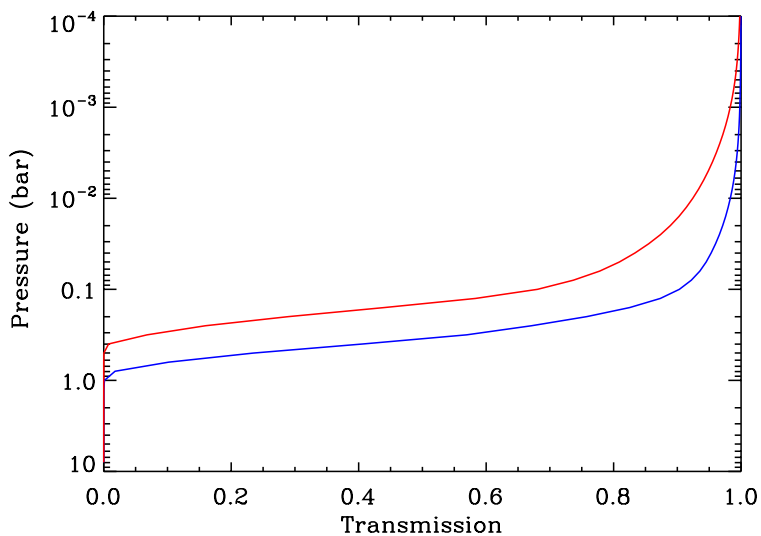


Fig. 6.— The transmission of $1.563 \mu\text{m}$ radiation through the limb of XO-2b as a function of the distance from the planet’s center defined by the pressure at the impact radius. Shown are the transmission of a model atmosphere for a radius of 0.942 (blue) and 0.952 (red).

Constraints on gas abundances depend on whether the lines are in the weak or strong line limits. In the weak line limit the curve of growth (i.e. the absorption) depends linearly on the abundance. In this case, if the radius is increased by 1% and the optical depth at a given pressure level increases by 100, the gas abundances need to be decreased by 1/100 to bring the optical depth of the larger planet in agreement with that of the small planet. Strong lines affect the absorption as the square root of the abundance; in this case the gas abundances need to be decreased by a factor of 1/10000. In summary, mixing ratios derived from primary transit data are extremely sensitive to the uncertainty in the planet’s radius.

3.4. Test with full model of XO-2b

The approximation above does not consider the dependence of the molecular cross section with pressure and temperature, which can be considerable. To evaluate these effects, we calculate a full radiative transfer model of XO-2b’s HST primary spectrum. This spectrum indicates primarily water absorption features (Crouzet et al. 2013), allowing us to simplify this exercise and consider absorption of water only, although other gases could be included as well. Several models are calculated, each with the radius altered by roughly 1.05% (700 km or $0.01R_J$) from an estimated value of $0.954 R_J$ (Fig. 7). A change of 700 km is equivalent to 2.3 atmospheric scale heights.⁴ For each model the gas abundance is recalculated to match the data (Fig. 7). The results of the radiative transfer models show that a 1% change in the XO-2b’s radius leads to an inferred abundance that differs from the original value by a factor of ~ 10 for mixing ratios of $10^{-8} - 10^{-6}$ and by a factor of ~ 100 for $[\text{H}_2\text{O}] = 10^{-6} - 10^{-2}$, consistent with the progression from the weak to strong line limits.

Let us compare this calculation with what we would expect from our simple approximation (Eq. 8). First we need to determine if the absorption through the limb of the planet obeys the strong or weak line limit. This can be accomplished by studying the dependence of the effective absorption ($-\ln(Tr)/N_T(R)$) through the limb on the assumed water mixing ratio.⁵ The effective absorption at $1.56 \mu\text{m}$ for water mixing ratios of $[\text{H}_2\text{O}] = 10^{-4}$ and 10^{-5} (Fig. 8) indicate two different regimes, depending on the pressure of the impact radius. For values less than $\sim 10^{-3}$ bars, the effective absorption of the $[\text{H}_2\text{O}] = 10^{-4}$ and 10^{-5} models differ by a factor of 10; here in the outer limb the absorption depends linearly on the mixing ratio. Deeper down, at pressures below 0.01

⁴The scale height of the exoplanet XO-2b is ~ 300 km, larger than that of the 1000 K hot Jupiter considered above, because XO-2b is roughly half the size of Jupiter. This study assumes $M_{\text{XO2b}} = 0.566 M_{\text{Jup}}$, (Torres et al. 2008), although a newer study indicates a value of $0.62 M_{\text{Jup}}$ (Narita et al. 2011), the $\sim 10\%$ difference of which does not significantly affect this analysis. We assume a value of 71000 km for the radius of Jupiter.

⁵We work with an “effective absorption” because the extinction is calculated from k-coefficients.

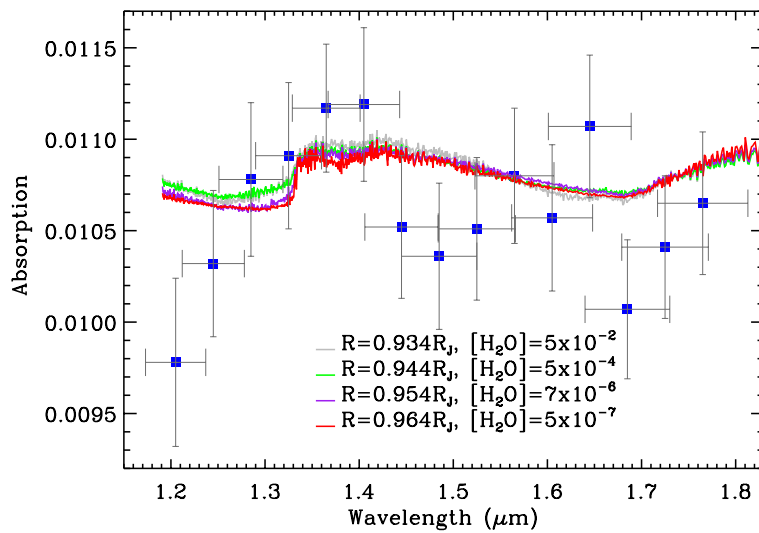


Fig. 7.— HST primary transit measurements of XO-2b (Crouzet et al. 2013) compared to models calculated for radii that differ consecutively by 1.05%. To produce similar spectra the water gas abundances were changed by factors of 14, 71 and 100, as the radius increases in value. The increased factor in the mixing ratio results from the line regime, which progresses from the weak line limit to the strong line limit as the gas abundance increases. (These models are not necessarily solutions, as the radius, composition and thermal profile must match both the emission and optical transmission data.)

bar, the absorption differs by $\sqrt{10} \sim 3$ (Fig. 3). For the pressure level probed at $1.56 \mu\text{m}$, $P_p \sim 0.5$ bars (Fig. 1), absorption obeys the strong line limit (Fig. 8).

Based on Eq. 8, an increase in XO-2b’s radius by 1%, the equivalent of 2.3 scale heights, requires that the optical depth be adjusted downward by a factor of 10 to produce the same spectrum. Since the transmission spectrum probes levels below $\sim 10^{-3}$ bars, absorption follows the strong line limit for water abundances of 10^{-5} – 10^{-4} bars. Our approximation therefore indicates that the water mixing ratios greater than 10^{-5} must be decreased by a factor of 1/100 to fit the data, if the radius is increased by 1%. This result agrees with that of the full model (Fig. 7) and indicates that the certainty in the derivation of composition of a planet’s atmosphere from primary transit data depends strongly on the precision with which the radius is known. For many planets this value is not well known; for example the radius of one of the most extensively measured exoplanet, HD189458b, is uncertain by 6% (Torres et al. 2008).

3.5. Temperature dependence on primary transit retrievals

The derived composition of an exoplanet is also sensitive to the assumed temperature structure through its effects on the atmospheric density structure and on the extinction coefficient. A cooler atmosphere is more compressed (smaller scale height) and exhibits a smaller light curve depth than does an otherwise identical warmer atmosphere. As a result, uncertainties in the temperature structure of an atmosphere lead to uncertainties in the abundance.

This sensitivity can be estimated roughly by calculating the impact radius where the traverse transmission $Tr = 0.5$ for a hot and cool planet; that is the radius, R_0 , where the atmosphere becomes optically thick. We consider, as an example, the effect of a 300 K uncertainty in the temperature profile, which is roughly that derived from studies of the dayside emission of HD 189733b (Madhusudhan & Seager 2009). At the wavelength $0.45 \mu\text{m}$, where the atmosphere’s opacity is dominated by Rayleigh scattering, the extinction coefficient is $\kappa_e = 2.4 \times 10^{-27} \text{ m}^2/\text{molecule}$. At this wavelength and assuming the ideal gas law and Eq. 5, a hot isothermal Jupiter exoplanet with $T = 1000\text{K}$, $M = M_J$, $R_r = R_J$, and $H=146 \text{ km}$, has a transverse chord transmission of 0.5 at 0.049 bar. This pressure level lies 776 km above our 10 bar reference level, R_p . If the temperature is increased everywhere by 300 K, i.e. to 1300 K, the scale height becomes 190 km. We find that the $Tr=0.5$ chord transmission occurs at 0.056 bar, which lies 983 km above the 10 bar level. The radius of the planet increased by 207 km. In order to achieve a transmission of 0.5 at the same radius, the optical depth of the hotter model must be decreased to one fourth the original value (Eq. 8) so that the radius decreased by 207 km. This estimate is of course rough, as we have assumed an isothermal atmosphere and considered only one absorption coefficient.

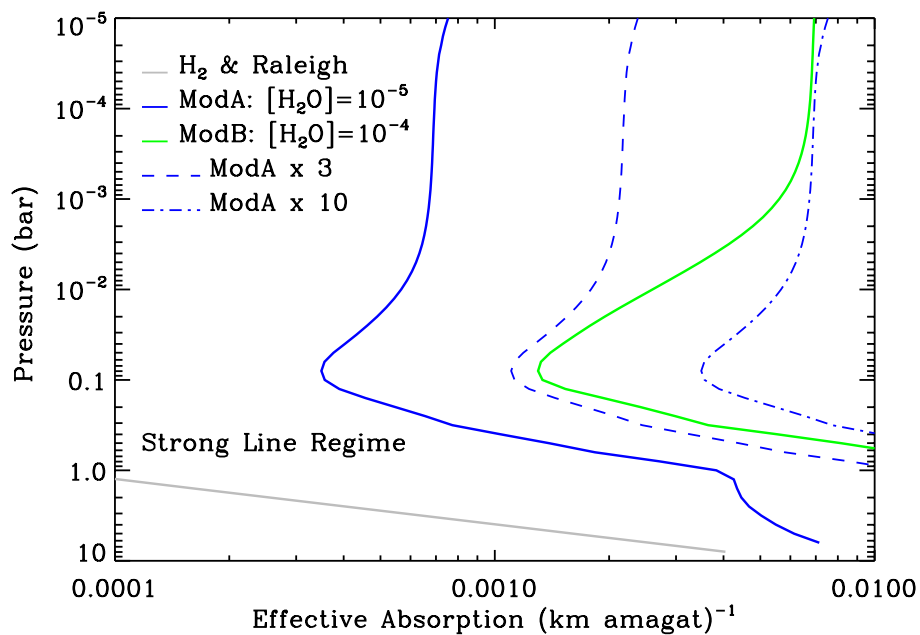


Fig. 8.— The effective absorption through the limb of XO-2b as a function of the impact radius for two model atmospheres of XO-2b (blue and green solid lines). These models are equivalent except that the green model has an order of magnitude less water than the blue model. Above a pressure of $\sim 10^{-3}$ bars, the absorption coefficients of the green model resemble those of the blue model divided by 10; here absorption follows the weak line regime. Below 0.01 bar the green model absorption coefficients follow those of the blue model divided by the $\sqrt{10} = 3$; here absorption follows the weak line limit.

To explore these effects further, a full radiative transfer model of XO-2b is compared to an analytical approximation, like that above. Considering first the analytical approach, the pressure level of the $Tr=0.5$ transmission at $0.45 \mu\text{m}$ wavelength for XO-2b is approximated (using Eq. 5) to be 0.04 bar, assuming a ballpark temperature of 1000 K and the atmospheric scale height of 300 km of XO-2b. A 300 K warmer planet has a $Tr=0.5$ transmission at 0.045 bar and the distance between the 10 bar level and the $Tr=0.5$ transmission level increased by 351 km (Eq. 8). At near-IR wavelengths, given the probed temperatures and pressures, the effective extinction coefficients range from values similar to that at $0.45 \mu\text{m}$ to values in the more transparent regions that are roughly 10 times less, e.g. $\kappa_e = 2.4 \times 10^{-28} \text{ m}^2/\text{molecule}$, at a spectral resolution of $R \sim 50$. Assuming this absorption, the transverse chord has a $Tr=0.5$ transmission at 0.46 bar (Eq. 5). A 300 K warmer planet has a $Tr=0.5$ transmission at 0.40 bar (Eq. 8), and the distance between the 10 bar level and the $Tr=0.5$ transmission level increased by 187 km. If primary transit data exists at $0.45 \mu\text{m}$, R_p is decreased so that the hot model fits the data, in which case the hot model's radius is too low to fit the near-IR data by $164 \text{ km} = 351 - 187$. In order to interpret both the optical and more transparent IR data the optical depth of the hotter model must be increased to half the original value (Eq. 8). Therefore, since the strong line limit applies, the mixing ratio must increase by a factor of 2–4, in the spectral regions that are most transparent depending on whether one is in the strong or weak line limit.

Considering now a full model atmosphere, the cooler model is assumed to have a temperature of 600 K above the 0.1 bar tropopause pressure and a 2500 K temperature below 2.8 bar. The warmer model is everywhere hotter by 300 K. We find that a hotter model, where temperatures are everywhere hotter by 300 K, indicates gas abundances that are 1.5 to 3 times greater compared the abundances indicated in the cooler model. This calculation agrees, within a factor of a few, with the analytical model. Thus uncertainties in the temperature profile affect the precision of the derived composition, however less significantly than do the uncertainties in the radius.

4. Resolving the Degeneracies

4.1. Determination of the radius

The study above indicates that derivations of composition of hot jovian exoplanets, while sensitive to the inferred temperature profile, are extremely contingent on the assumed planetary radius as a function of pressure. Errors in the derived radius arise from two sources: 1) uncertainties in the measured radius of the roughly unity optical depth, e.g. (Torres et al. 2008); and 2) uncertainties in the assignment of the pressure level associated with the retrieved radius at unity optical depth. These uncertainties, on the level of a few percent of the planet's radius (i.e. over 1000 km), exceed

the range of radii that are currently considered in most inversion studies of exoplanetary spectra.

High spectral resolution observations of Solar System planets resolve the pressure of an absorption feature through the line widths of absorption features, which are established by pressure broadening in the troposphere. Yet this technique does not work as well for hot jupiter atmospheres, which are hot enough that doppler broadening establishes the line widths over most of the observable atmosphere.⁶ In addition, the faint nature of exoplanets hinders high resolution spectroscopy.

A more appropriate method for eliminating degenerate solutions to the primary transit data is to measure the radius at a wavelength where the atmosphere’s opacity, and thus the probed pressure level, is known (Lecavelier Des Etangs et al. 2008; Benneke & Seager 2012). For the atmospheres of hot jovian exoplanets the region between 0.3–0.5 μm is defined mainly by Rayleigh scattering, as long as the atmosphere is cloudless. If the atmosphere is cloudy, such measurements define the upper limit of the radius at a specific pressure, since clouds add an unknown opacity source. For the brightest exoplanets, radii can be constrained using U ($\lambda \sim 0.35 \mu\text{m}$) and B ($\lambda \sim 0.45 \mu\text{m}$) photometry with relatively small telescopes (e.g. 1.6 m) equipped with a sensitive CCD and a high cadence readout (Dittmann et al. 2009; Turner et al. 2013; Teske et al. 2013b). In addition star spots, which can considerably affect optical measurements, can be characterized through broad-band optical and near-IR photometry (Ballerini et al. 2012). Larger ground-based telescopes are able to obtain optical spectra, which have the advantage of defining the slope of the opacity and thus potentially the distinctive Rayleigh signature, which indicates gas scattering as opposed to that of clouds or haze. Small telescope optical observations of exoplanets outside of absorption features such as Na and K probe spectral regions where the primary opacity of the atmosphere, if cloud free, is known. Observations at these wavelengths constrain the radius pertaining to a specific pressure level, thereby enabling interpretations of IR primary transit measurements from HST, Spitzer and ground-based platforms. This leverage can be seen in the analysis of primary transit and secondary eclipse data of XO-2b (Griffith et al. 2013).

4.2. Joint analysis of primary and secondary transits

The first optical photometry of XO-2b, conducted in the broad Sloan z band (effectively $\sim 0.83\text{--}1.00 \mu\text{m}$), yielded a measurement of the planet’s density and radius of $0.996 R_J$, corre-

⁶ The doppler broadening full width half maximum (FWHM) of a 1000 K atmosphere exceeds the pressure broadening FWHM (assuming a standard STP value of 0.05 cm^{-1}) at all wavelengths below $4 \mu\text{m}$ and all pressures less than 1 bar. Since the pressure broadening FWHM depends linearly with pressure, Doppler broadening dominates over pressure broadening for hot Jupiters except at high wavelengths that probe deep levels.

sponding to the level where the tangent chord is optically thick over the wavelengths sampled (Fernandez et al. 2009). It is difficult to associate this radius to a pressure level because the band covers spectral features due to K (Sing et al. 2012), Na and water. Griffith et al. (2013) therefore recorded photometry of XO-2b at the 1.55 meter Kuiper Telescope on Mt. Bigelow in the U-band and B-bands, outside the effects of atomic and molecular spectral features, where Rayleigh scattering establishes the opacity, if cloud-free. Data were obtained between January 2012 and February 2013 over the course of 4 nights, yielding 3 measurements of the U band (0.303–0.417 μm) and 2 of the B band (0.33–0.55 μm) (Griffith et al. 2013). Here we consider the data from 9 December 2012, the one night in which both U and B measurements were simultaneously recorded (Fig. 9), and discuss the implications of the other measurements below.

The observations are analyzed to determine the planetary radius at 10 bar, which depends on the thermal profile. The range of values that fit the U and B data span about 1% of the planetary radius (Fig. 9), causing, according to our approximations, an uncertainty of a factor of 100 in the derived abundance assuming a fixed temperature profile. However since the temperature is not constrained there is a larger range of solutions. The temperature profiles that fit the secondary eclipse data range by 1000 K, suggesting an uncertainty of roughly an order of magnitude in the derived gas abundances from the primary eclipse due to the temperature range for a given assumed radius. But then the radius that fits the data depends on the temperature profile, as also demonstrated in models of test hot Jupiter spectra (Barstow et al. 2013). These considerations indicate the difficulty in deriving constraints from either primary or secondary eclipse data alone, and point to a coupled analysis of both emission and transmission data. In fact, such an analysis, described below, shows that coupled temperature and abundance profiles derived from the secondary eclipse data can form quite a separate solution set from that of the primary transit data, which overlap in a small region of phase space.

To interpret both primary transit and secondary eclipse data we begin by assuming cloudless conditions. First the radius, R_p , is determined from the U and B band light curves separately for each thermal profile considered in the analysis of the secondary eclipse measurements of (Machalek et al. 2009). Analyses of the secondary eclipse data provide a solution set of coupled thermal profiles and composition (e.g. Fig. 3). These models are fed into a calculation of the primary transit light curves depths, which are compared to the near-IR transmission data (Crouzet et al. 2013) to determine the models that matches both secondary and primary eclipse measurements (Figs. 1 & 9). The solution set is calculated for both the largest and smallest radii to derive models that interpret all the data within errors. This analysis yields significantly stronger constraints on the water composition of XO-2b than does the interpretation of one type of data alone, as shown for water in Fig. 10.

The differences between the terminator and the dayside hemisphere compositions (sampled

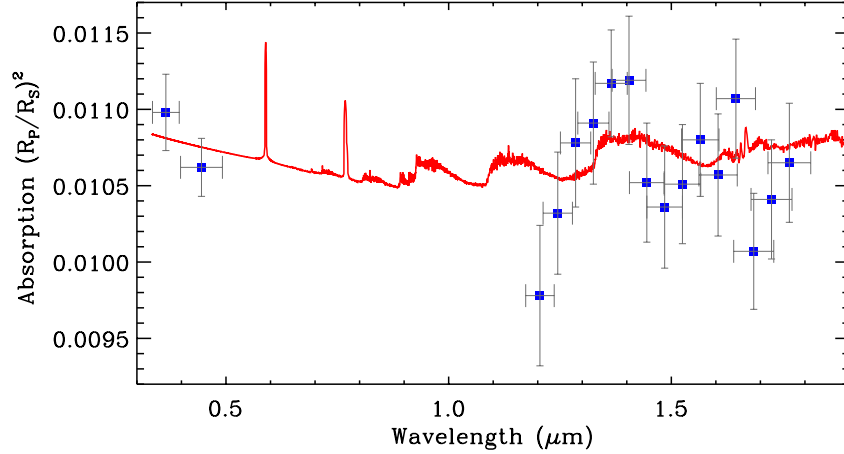


Fig. 9.— Primary transit near-IR spectrum (Crouzet et al. 2013) and optical photometry measurements (Griffith et al. 2013) of XO-2b (blue squares) are compared to a model spectrum (red).

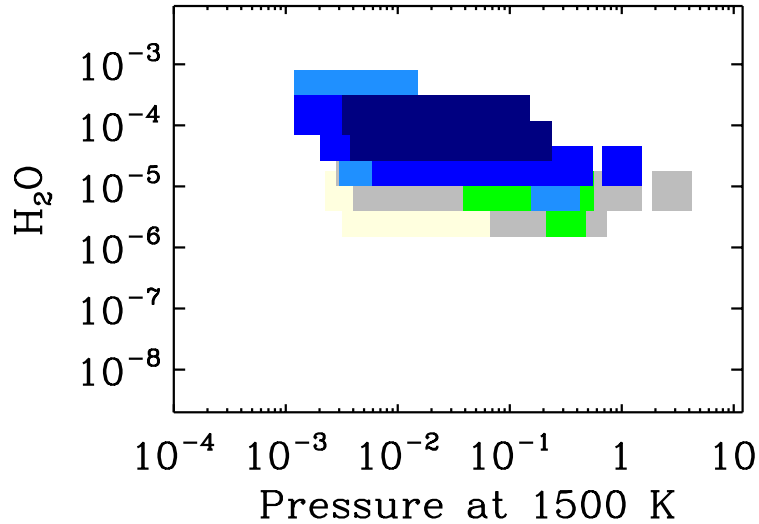


Fig. 10.— The subset of models that fit both the emission and transmission measurements of XO-2b. The blue squares indicate the best fits to the primary transit spectrum (Griffith et al. 2013).

during primary transit and secondary eclipse respectively) depends on the species and pressure level probed. Water, which likely dominates XO-2b's spectrum, and CO are expected to have constant abundances over the pressure levels probed, both vertically and horizontally, as they are not affected by photochemistry below $\sim 10^{-6}$ bars. Methane and carbon dioxide, more strongly affected by photochemistry, are predicted to have variable vertical profiles (Moses et al. 2011), which, with low spectral resolution observations, are measured as weighted average abundances over the small pressure regions probed. These species also vary in abundance between the terminator to dayside atmosphere depending on the insolation and vertical mixing. For example, predictions for HD 189733b lead to the hemispherical abundances that differ by factors of ~ 4 and < 2 , for methane and carbon dioxide, respectively (Moses et al. 2011). Jovian exoplanets, which are mostly locked in synchronous rotation about their host stars, also display different temperature profiles (Fig. 2) at the terminator compared to the dayside atmosphere (Harrington et al. 2006; Knutson et al. 2007; Crossfield et al. 2010; Knutson et al. 2012; Lewis et al. 2013). Models of the thermal profiles of the close analog system HD 189458b indicate dayside temperatures 100-200 K hotter than those at the terminator (Showman et al. 2009), which, based on our estimates, leads to an overestimate in the gas abundances derived by the primary transit data by a factor of 1-2.

Clouds have different effects on primary eclipse data depending on the cloud particle sizes. One can envision two possible scenarios. The clouds could be of roughly uniform optical thickness from optical to IR wavelength if the cloud particle size exceeds $10\mu\text{m}$. An example is the water clouds on Earth. Alternatively, clouds could be more optically thick at shorter wavelengths rather than at longer wavelengths if they consist of sub-micron sized particles. Such particles describe the photochemical haze on Titan (Tomasko et al. 2008). The presence of the former large particle clouds would increase the exoplanet's radius at wavelengths that probe down to the cloud deck. The model of the primary transit spectrum would be flattened, contrary to what we observe. The presence of the latter small particle clouds would increase the light curve depth at small wavelengths, with no effect on the near-IR spectrum. In this case, the inferred gas abundances would be larger than those determined for a cloudless atmosphere. The entire solution set would shift upward, and the abundance of water could be higher than that expected for a solar metallicity atmosphere in thermochemical equilibrium. Since the existence of such a cloud cannot be discounted in this case, the measurement of XO-2b radius is in fact an upper limit, since the presence of a cloud would indicate a smaller radius. The upper limit of XO-2b's radius allows one to constrain the lower limit of the gas abundances.

The additional U and B measurements are particularly interesting because they indicate the effects of processes that have not been considered in the analysis above. Specifically the measurement in the B band on 28 October 2012 disagrees with that from 9 December 2012 at the three sigma level (Griffith et al. 2013). Regarding the two remaining U values, the radius derived from the 5 Jan 2012 data is identical to that of 9 December 2012, while the 23 Feb 2013 value is higher

by roughly 1 sigma (Griffith et al. 2013). A more extensive discussion of the errors and their treatment is given in (Griffith et al. 2013). The spurious U value may result either from the presence of non-uniform clouds in XO-2b’s atmosphere or from sunspots on the host star. Unaccounted for systematic errors in the data could also play a role. The higher radius derived from the outlying B and U measurements allow for a significantly larger solution set in the analysis of the secondary and primary measurements (Griffith et al. 2013). In addition, they introduce the possibility that observations taken at different times, and therefore potentially different cloud or sunspot conditions, cannot be interpreted together. The cause of the the variability in the measured flux can be investigated by optical spectra, which will yield the slope of the primary eclipse spectrum and thus whether due to gas or cloud scattering. Simultaneous photometric measurements from a number of telescopes will further illuminate the systematic errors.

5. Summary

The analysis of a sparse data set discussed above indicates that future prospects are promising: the primary transit and secondary eclipse data considered together can, with greater spectral coverage and sampling, lead to strong constraints on the characteristics of exoplanet atmospheres. However this exercise also indicates a lack of vital information that is needed to constrain the exoplanet characteristics. The rigor of the approach outlined here would be improved with full phase observations which illuminates disk variations in the temperature and composition profiles, (e.g. Knutson *et al.* 2012, Lewis *et al.* 2013). The exoplanet’s atmosphere was assumed, for lack of information, to be cloudless, although in fact, the variability in the measurements potentially points to variable cloud cover. As indicated by measurements of brown dwarfs(e.g. Kirkpatrick *et al.* 2005) and the directly measured HR8799 planets (e.g. Marois *et al.* 2008, Marois *et al.* 2010) observations of cloud effects depend on the gravity, effective temperature and thus the sedimentation efficiency of the planet (Marley et al. 2012). In addition, we assumed no temperature inversion (i.e. as in a stratosphere) and no non-LTE emission, both of which can effect specific features. Observations in the L-band of HD 189733b indicate non-LTE emission (Swain et al. 2010; Waldmann et al. 2012), and HD 209458b’s spectrum indicates the presence of a stratosphere (Burrows et al. 2007; Madhusudhan & Seager 2009). The interpretation of transiting planet measurements are also potentially affected by star spots, which are indicated by measurements of the host star HD 189733, (e.g. Pont *et al.* 2007, MillerRicci *et al.* 2008). In addition, many analyses of exoplanetary data, including the primary transit measurements discussed here, do not fit all of the data to within the error bars (Fig. 9).

Smaller and cooler planets more similar to Earth present more challenges. As poor emitters, they cannot presently be measured with secondary eclipse observations. One cannot assume the

composition of the primary constituent, and thus the mean molecular weight as we did here. Also, the presence of a surface adds an additional variable to be investigated. As explored by models of Benneke and Seager (2012), these additional challenges can be addressed by recording high signal to noise spectra over a broad wavelength region ($0.5\text{--}5\ \mu\text{m}$), possible for some planets with upcoming James Web Space Telescope (JWST) (Benneke & Seager 2012). The lack of secondary eclipse spectra is treated by making assumptions regarding a radiative-convective thermal profile, based on albedo assumptions (Benneke & Seager 2012). The mean molecular weight is decoupled from the derivation of other parameters by recording both weak and strong lines of the same constituent, the radius and Rayleigh slope from high S/N data extending from $0.4\text{--}0.7\ \mu\text{m}$, and the wavelength shift in the Rayleigh slope (Benneke & Seager 2012). Detailed studies of smaller and cooler planets may be best approached with large mirror investigations, e.g. with the JWST.

However, the combined analysis of primary and secondary eclipse data and the exploration of the degeneracy of solutions explored here indicates the need to better understand exoplanet data, the properties of host stars, and the range of assumptions inherent in any model. This task requires observations from ground and space of many extrasolar systems. A small space telescope survey of exoplanets, where each observation covers large wavelength IR region with redundant molecular features with sufficient resolution to identify broad rotation-vibrational features, would constrain a significant number of basic parameters of hundreds of systems. Multiple observations of planetary systems from ground-based telescopes can explore time-variable processes such as clouds and star spots. In addition, there is a need to target exoplanets of particular interest with large telescopes, which perforce will not have the time to sample a large number of planetary systems. This combined approach of survey telescopes and large mirror telescopes in space, will provide detailed information on particular systems, and general information on a large number of systems, as needed to understand planet formation explore and the variety of planets and planetary systems.

REFERENCES

- Ballerini, P., Micela, G., Lanza, A. F., & Pagano, I. 2012, *A&A*, 539, A140
- Barstow, J. K., Aigrain, S., Irwin, P. G. J., Bowles, N., Fletcher, L. N., & Lee, J.-M. 2013, *MNRAS*, 430, 1188
- Benneke, B., & Seager, S. 2012, *ApJ*, 753, 100
- Brown, T. M. 2001, *ApJ*, 553, 1006
- Burke, C. J., McCullough, P. R., Valenti, J. A., Johns-Krull, C. M., Janes, K. A., Heasley, J. N., Summers, F. J., Stys, J. E., Bissinger, R., Fleenor, M. L., Foote, C. N., García-Melendo, E.,

- Gary, B. L., Howell, P. J., Mallia, F., Masi, G., Taylor, B., & Vanmunster, T. 2007, *ApJ*, 671, 2115
- Burrows, A., Hubeny, I., Budaj, J., Knutson, H. A., & Charbonneau, D. 2007, *ApJ*, 668, L171
- Chamberlain, J. W., & Hunten, D. M. 1988, Academic Press, 41, 481
- Charbonneau, D., Allen, L. E., Megeath, S. T., Torres, G., Alonso, R., Brown, T. M., Gilliland, R. L., Latham, D. W., Mandushev, G., O'Donovan, F. T., & Sozzetti, A. 2005, *ApJ*, 626, 523
- Charbonneau, D., Brown, T. M., Latham, D. W., & Mayor, M. 2000, *ApJ*, 529, L45
- Cho, J. Y.-K., Menou, K., Hansen, B. M. S., & Seager, S. 2003, *ApJ*, 587, L117
- Crossfield, I. J. M., Hansen, B. M. S., Harrington, J., Cho, J. Y.-K., Deming, D., Menou, K., & Seager, S. 2010, *ApJ*, 723, 1436
- Crouzet, N., McCullough, P. R., Burke, C., & Long, D. 2013, arXiv, xx
- Deming, D., Seager, S., Richardson, L. J., & Harrington, J. 2005, *Nature*, 434, 740
- Dittmann, J. A., Close, L. M., Green, E. M., Scuderi, L. J., & Males, J. R. 2009, *ApJ*, 699, L48
- Fernandez, J. M., Holman, M. J., Winn, J. N., Torres, G., Shporer, A., Mazeh, T., Esquerdo, G. A., & Everett, M. E. 2009, *AJ*, 137, 4911
- Fortney, J. J., Marley, M. S., Lodders, K., Saumon, D., & Freedman, R. 2005, *ApJ*, 627, L69
- Fortney, J. J., Shabram, M., Showman, A. P., Lian, Y., Freedman, R. S., Marley, M. S., & Lewis, N. K. 2010, *ApJ*, 709, 1396
- Fressin, F., Torres, G., Charbonneau, D., Bryson, S. T., Christiansen, J., Dressing, C. D., Jenkins, J. M., Walkowicz, L. M., & Batalha, N. M. 2013, *ApJ*, 766, 81
- Griffith, C. A., Turner, J. D., Zellem, R., & Teske, J. K. 2013, *ApJ*, Submitted, xxx
- Grillmair, C. J., Burrows, A., Charbonneau, D., Armus, L., Stauffer, J., Meadows, V., van Cleve, J., von Braun, K., & Levine, D. 2008, *Nature*, 456, 767
- Harrington, J., Hansen, B. M., Luszcz, S. H., Seager, S., Deming, D., Menou, K., Cho, J. Y.-K., & Richardson, L. J. 2006, *Science*, 314, 623
- Knutson, H. A., Charbonneau, D., Allen, L. E., Fortney, J. J., Agol, E., Cowan, N. B., Showman, A. P., Cooper, C. S., & Megeath, S. T. 2007, *Nature*, 447, 183

- Knutson, H. A., Lewis, N., Fortney, J. J., Burrows, A., Showman, A. P., Cowan, N. B., Agol, E., Aigrain, S., Charbonneau, D., Deming, D., Désert, J.-M., Henry, G. W., Langton, J., & Laughlin, G. 2012, *ApJ*, 754, 22
- Lecavelier Des Etangs, A., Vidal-Madjar, A., Désert, J.-M., & Sing, D. 2008, *A&A*, 485, 865
- Lee, J.-M., Fletcher, L. N., & Irwin, P. G. J. 2012, *MNRAS*, 420, 170
- Lewis, N. K., Knutson, H. A., Showman, A. P., Cowan, N. B., Laughlin, G., Burrows, A., Deming, D., Crepp, J. R., Mighell, K. J., Agol, E., Bakos, G. Á., Charbonneau, D., Désert, J.-M., Fischer, D. A., Fortney, J. J., Hartman, J. D., Hinkley, S., Howard, A. W., Johnson, J. A., Kao, M., Langton, J., & Marcy, G. W. 2013, *ApJ*, 766, 95
- Line, M. R., Zhang, X., Vasisht, G., Natraj, V., Chen, P., & Yung, Y. L. 2012, *ApJ*, 749, 93
- Machalek, P., McCullough, P. R., Burrows, A., Burke, C. J., Hora, J. L., & Johns-Krull, C. M. 2009, *ApJ*, 701, 514
- Madhusudhan, N., Burrows, A., & Currie, T. 2011, *ApJ*, 737, 34
- Madhusudhan, N., & Seager, S. 2009, *ApJ*, 707, 24
- Marley, M. S., Saumon, D., Cushing, M., Ackerman, A. S., Fortney, J. J., & Freedman, R. 2012, *ApJ*, 754, 135
- Miller-Ricci, E., Seager, S., & Sasselov, D. 2009, *ApJ*, 690, 1056
- Moses, J. I., Visscher, C., Fortney, J. J., Showman, A. P., Lewis, N. K., Griffith, C. A., Klippenstein, S. J., Shabram, M., Friedson, A. J., Marley, M. S., & Freedman, R. S. 2011, *ApJ*, 737, 15
- Narita, N., Hirano, T., Sato, B., Harakawa, H., Fukui, A., Aoki, W., & Tamura, M. 2011, *PASJ*, 63, L67
- Nassar, R., & Bernath, P. 2003, *Journal of Quantitative Spectroscopy and Radiative Transfer*, 82, 279
- Rodgers, C. D. 2000, Singapore: World Scientific Publishing, 00,
- Rothman, L. S., Gordon, I. E., Barbe, A., Benner, D. C., Bernath, P. F., Birk, M., Boudon, V., Brown, L. R., Campargue, A., Champion, J.-P., Chance, K., Coudert, L. H., Dana, V., Devi, V. M., Fally, S., Flaud, J.-M., Gamache, R. R., Goldman, A., Jacquemart, D., Kleiner, I., Lacome, N., Lafferty, W. J., Mandin, J.-Y., Massie, S. T., Mikhailenko, S. N., Miller, C. E.,

- Moazzen-Ahmadi, N., Naumenko, O. V., Nikitin, A. V., Orphal, J., Perevalov, V. I., Perrin, A., Predoi-Cross, A., Rinsland, C. P., Rotger, M., Šimečková, M., Smith, M. A. H., Sung, K., Tashkun, S. A., Tennyson, J., Toth, R. A., Vandaele, A. C., & Vander Auwera, J. 2009, *Journal of Quantitative Spectroscopy and Radiative Transfer*, 110, 533
- Seager, S., & Sasselov, D. D. 2000, *ApJ*, 537, 916
- Showman, A. P., Fortney, J. J., Lian, Y., Marley, M. S., Freedman, R. S., Knutson, H. A., & Charbonneau, D. 2009, *ApJ*, 699, 564
- Sing, D. K., Huitson, C. M., Lopez-Morales, M., Pont, F., Désert, J.-M., Ehrenreich, D., Wilson, P. A., Ballester, G. E., Fortney, J. J., Lecavelier des Etangs, A., & Vidal-Madjar, A. 2012, *MNRAS*, 426, 1663
- Swain, M. R., Deroo, P., Griffith, C. A., Tinetti, G., Thatte, A., Vasisht, G., Chen, P., Bouwman, J., Crossfield, I. J., Angerhausen, D., Afonso, C., & Henning, T. 2010, *Nature*, 463, 637
- Swain, M. R., Tinetti, G., Vasisht, G., Deroo, P., Griffith, C., Bouwman, J., Chen, P., Yung, Y., Burrows, A., Brown, L. R., Matthews, J., Rowe, J. F., Kuschnig, R., & Angerhausen, D. 2009, *ApJ*, 704, 1616
- Tashkun, S. A., Perevalov, V. I., Teffo, J.-L., Bykov, A. D., & Lavrentieva, N. N. 2003, *Journal of Quantitative Spectroscopy and Radiative Transfer*, 82, 165
- Teske, J. K., Schuler, S. C., Cunha, K., Smith, V. V., & Griffith, C. A. 2013a, *ApJ*, 768, L12
- Teske, J. K., Turner, J. D., Mueller, M., & Griffith, C. A. 2013b, *MNRAS*, 431, 1669
- Thiévin, J., Georges, R., Carles, S., Benidar, A., Rowe, B., & Champion, J. 2008, *Journal of Quantitative Spectroscopy and Radiative Transfer*, 109, 2027
- Tinetti, G., Deroo, P., Swain, M. R., Griffith, C. A., Vasisht, G., Brown, L. R., Burke, C., & McCullough, P. 2010, *ApJ*, 712, L139
- Tinetti, G., Vidal-Madjar, A., Liang, M.-C., Beaulieu, J.-P., Yung, Y., Carey, S., Barber, R. J., Tennyson, J., Ribas, I., Allard, N., Ballester, G. E., Sing, D. K., & Selsis, F. 2007, *Nature*, 448, 169
- Tomasko, M. G., Doose, L., Engel, S., Dafoe, L. E., West, R., Lemmon, M., Karkoschka, E., & See, C. 2008, *Planet. Space Sci.*, 56, 669
- Torres, G., Winn, J. N., & Holman, M. J. 2008, *ApJ*, 677, 1324

Turner, J. D., Smart, B. M., Hardegree-Ullman, K. K., Carleton, T. M., Walker-LaFollette, A. M., Crawford, B. E., Smith, C.-T. W., McGraw, A. M., Small, L. C., Rocchetto, M., Cunningham, K. I., Towner, A. P. M., Zellem, R., Robertson, A. N., Guvenen, B. C., Schwarz, K. R., Hardegree-Ullman, E. E., Collura, D., Henz, T. N., Lejoly, C., Richardson, L. L., Weinand, M. A., Taylor, J. M., Daugherty, M. J., Wilson, A. A., & Austin, C. L. 2013, *MNRAS*, 428, 678

Waldmann, I. P., Tinetti, G., Drossart, P., Swain, M. R., Deroo, P., & Griffith, C. A. 2012, *ApJ*, 744, 35